IOP Publishing | International Atomic Energy Agency Nuclear Fusion
Nucl. Fusion **54** (2014) 104012 (13pp) doi:10.1088/0029-5515/54/10/104012

Multi-phase simulation of fast ion profile flattening due to Alfvén eigenmodes in a DIII-D experiment

Y. Todo[1,2], M.A. Van Zeeland[3], A. Bierwage[4] and W.W. Heidbrink[5]

[1] National Institute for Fusion Science, Toki, Japan
[2] Department of Fusion Science, The Graduate University for Advanced Studies (SOKENDAI), Toki, Japan
[3] General Atomics, San Diego, CA, USA
[4] Japan Atomic Energy Agency, Rokkasho, Japan
[5] Department of Physics and Astronomy, University of California, Irvine, CA, USA

E-mail: todo@nifs.ac.jp

Received 16 November 2013, revised 2 May 2014
Accepted for publication 6 May 2014
Published 1 October 2014

Abstract

A multi-phase simulation that is a combination of classical simulation and hybrid simulation for energetic particles interacting with a magnetohydrodynamic (MHD) fluid is developed to simulate the nonlinear dynamics on the slowing down time scale of the energetic particles. The hybrid simulation code is extended with realistic beam deposition profile, collisions and losses, and is used for both the classical and hybrid phases. The code is run without MHD perturbations in the classical phase, while the interaction between the energetic particles and the MHD fluid is simulated in the hybrid phase. In a multi-phase simulation of DIII-D discharge #142111, the stored beam ion energy is saturated due to Alfvén eigenmodes (AE modes) at a level lower than in the classical simulation. After the stored fast ion energy is saturated, the hybrid simulation is run continuously. It is demonstrated that the fast ion spatial profile is significantly flattened due to the interaction with the multiple AE modes with amplitude $v/v_A \sim \delta B/B \sim O(10^{-4})$. The dominant AE modes are toroidal Alfvén eigenmodes (TAE modes), which is consistent with the experimental observation at the simulated moment. The amplitude of the temperature fluctuations brought about by the TAE modes is of the order of 1% of the equilibrium temperature. This is also comparable with electron cyclotron emission measurements in the experiment.

Keywords: fast ion, energetic particle, Alfvén eigenmode, hybrid simulation

(Some figures may appear in colour only in the online journal)

1. Introduction

Significant flattening of the fast ion profile was observed during Alfvén eigenmode (AE mode) activity in DIII-D experiments [1]. In the experiments, a rich spectrum of toroidal Alfvén eigenmodes (TAE modes) and reversed shear Alfvén eigenmodes (RSAE modes) driven by ~80 keV neutral beam injection is observed during the current ramp-up phase with reversed magnetic shear. Much attention has been paid to the DIII-D experiments, and many theoretical studies have been devoted. Excellent agreement was found between ideal magnetohydrodynamic (MHD) NOVA predictions and electron cyclotron emission (ECE) measurements of the electron temperature fluctuation amplitude profile due to a TAE mode [2]. It was demonstrated with the ORBIT simulation that multiple low-amplitude AE modes with $\delta B/B \sim O(10^{-4})$ can account for significant modification of fast ion distributions [3, 4]. Fast ion induced shearing of two-dimensional AE mode profile was measured by ECE imaging and well described by the hybrid gyrofluid–MHD code TAEFL [5]. The scintillator detector measurements of fast ion losses due to AE modes were reproduced with the ORBIT code [6]. Stability of AE modes was investigated with the NOVA-K code, and good agreement was found with the spectrum of observed modes [7]. Three gyrokinetic simulation codes were validated on the frequency sweeping of an RSAE mode [8]. Nonlinear simulations have also been performed on the DIII-D experiments [9, 10].

For the fast ion transport investigated in [3, 4], resonance overlap was found to be the key mechanism. Resonance overlap of multiple AE modes was predicted to lead to global diffusion of fast ions and enhancement in the AE mode energy [11]. A reduced simulation reproduced TAE bursts and fast ion losses of a TFTR experiment [12]. The fast ion transport mechanism in that work was found to be resonance

overlap and overlap of higher order islands created by a single mode. However, the saturation amplitude in the simulation was $\delta B/B \sim 2 \times 10^{-2}$ at the mode peak locations, which is larger than that in the TFTR experiment by roughly one order of magnitude. A nonlinear MHD simulation with fast ion source and slowing down collisions demonstrated that the nonlinear MHD effect reduces the saturation amplitude for the TFTR experiment to $\delta B/B \sim 5 \times 10^{-3}$ at the mode peak locations, and $\delta B/B \sim 10^{-3}$ at the edge region, which is comparable to the experiment [13].

A question that arises is 'what is the required AE mode amplitude for considerable fast ion transport?' In the simulation for the TFTR experiment the saturation AE mode amplitude is $\delta B/B \sim 5 \times 10^{-3}$ at the mode peak locations, while the inferred amplitude is $\delta B/B \sim 10^{-4}$ in the DIII-D experiment. This difference might be attributed to the differences in temporal behaviour of AE modes (bursty in TFTR versus steady in DIII-D), and in q-profile (normal shear with $q_{\min} \sim 1$ in TFTR versus reversed shear with $q_{\min} \sim 3-4$ in DIII-D). However, a definite answer to this question is given only by the MHD simulation applied to the DIII-D experiment and motivates us to simulate the DIII-D experiment as realistically as possible.

2. Simulation model

2.1. Hybrid simulation model of energetic particles and MHD

Several hybrid simulation models have been constructed [14–18] to study the evolution of AE modes destabilized by energetic particles. In the MEGA code, the bulk plasma is described by the nonlinear MHD equations and the fast ions are simulated with the particle-in-cell method. The MHD equations with the fast ion effects are given by

$$\frac{\partial \rho}{\partial t} = -\nabla \cdot (\rho \boldsymbol{v}) + \nu_{\rm n} \Delta(\rho - \rho_{\rm eq}), \tag{1}$$

$$\rho \frac{\partial}{\partial t}\boldsymbol{v} = -\rho \vec{\omega} \times \boldsymbol{v} - \rho \nabla \left(\frac{v^2}{2}\right) - \nabla p + (\boldsymbol{j} - \boldsymbol{j}'_h) \times \boldsymbol{B} + \frac{4}{3}\nabla(\nu\rho \nabla \cdot \boldsymbol{v}) - \nabla \times (\nu\rho\vec{\omega}), \tag{2}$$

$$\frac{\partial \boldsymbol{B}}{\partial t} = -\nabla \times \boldsymbol{E}, \tag{3}$$

$$\frac{\partial p}{\partial t} = -\nabla \cdot (p\boldsymbol{v}) - (\gamma - 1) p \nabla \cdot \boldsymbol{v} + (\gamma - 1)\left[\nu\rho\omega^2 + \frac{4}{3}\nu\rho(\nabla \cdot \boldsymbol{v})^2 + \eta \boldsymbol{j} \cdot (\boldsymbol{j} - \boldsymbol{j}_{\rm eq})\right] + \chi \Delta(p - p_{\rm eq}), \tag{4}$$

$$\boldsymbol{E} = -\boldsymbol{v} \times \boldsymbol{B} + \eta(\boldsymbol{j} - \boldsymbol{j}_{\rm eq}), \tag{5}$$

$$\boldsymbol{j} = \frac{1}{\mu_0} \nabla \times \boldsymbol{B}, \tag{6}$$

$$\vec{\omega} = \nabla \times \boldsymbol{v}, \tag{7}$$

where μ_0 is the vacuum magnetic permeability, γ is the adiabatic constant, ν, $\nu_{\rm n}$ and χ are artificial viscosity and diffusion coefficients chosen to maintain numerical stability and all the other quantities are conventional. In this work, the dissipation coefficients ν, $\nu_{\rm n}$, χ and η/μ_0 are assumed to be equal to each other. The dissipation terms play a physical role to enhance the damping of AE modes in the MHD simulation that does not include kinetic damping such as radiative damping [19] and thermal ion Landau damping. We investigate three values of the coefficients, 5×10^{-7}, 2×10^{-6} and 5×10^{-6} normalized by $v_{\rm A} R_0$ where $v_{\rm A}$ is the Alfvén velocity at the plasma centre, and R_0 is the major radius at the geometrical centre of the simulation domain. The subscript 'eq' represents the equilibrium variables. The MHD momentum equation (equation (2)) includes the fast ion contribution in the fast ion current density $\boldsymbol{j}'_h$ that consists of the contributions from parallel velocity, magnetic curvature and gradient drifts, and magnetization current. The $\boldsymbol{E} \times \boldsymbol{B}$ drift disappears in $\boldsymbol{j}'_h$ due to the quasi-neutrality [20]. We see that the electromagnetic field is given by the standard MHD description. This model is accurate under the condition that the fast ion density is much less than the bulk plasma density. The MHD equations are solved using a fourth-order (in both space and time) finite difference scheme.

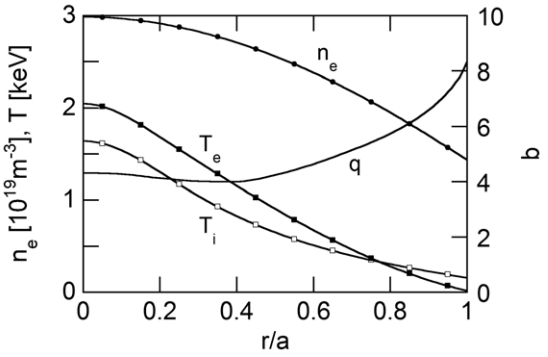

Figure 1. Radial profiles of equilibrium electron density ($n_{\rm e}$), electron temperature ($T_{\rm e}$), ion temperature ($T_{\rm i}$) and safety factor (q).

The fast ions are simulated using the particle-in-cell method, and a drift-kinetic description [21], where we employ the gyrokinetic approach to account for finite Larmor radius effects. The electromagnetic fluctuations are averaged over the fast ion gyro-orbit for the fast ion dynamics. Cylindrical coordinates (R, φ, z) are used in the simulation. For the purpose of the data analysis, magnetic flux coordinates (r, φ, ϑ) were constructed for the MHD equilibrium where r is the radial coordinate with $r = 0$ at the plasma centre and $r = a$ at the plasma edge, and ϑ is the poloidal angle. The equations of motion for each computational particle are solved using a fourth-order Runge–Kutta method.

2.2. Implementation of beam injection, collisions and losses

We investigate the nonlinear evolution of AE modes and beam ions in DIII-D discharge #142111 at $t = 525$ ms. The equilibrium is reconstructed with the EFIT code [22], and the relevant profiles are shown in figure 1. We assume a continuous and constant beam injection with a realistic beam ion deposition profile given by the TRANSP [23] code for $t = 525$ ms. In this work we introduce only the full-energy component with energy of approximately 80 keV. The beam deposition power is 4.95 MW, and is 79% of the total deposition power in the experiment that includes the half and third energy components. The beam deposition profile in (P_φ, Λ) space is shown in figure 2. Here, $P_\varphi = e_{\rm f}\psi + m_{\rm f} R v_\parallel b_\varphi$ is the toroidal canonical momentum defined with fast ion charge $e_{\rm f}$ and mass $m_{\rm f}$, poloidal magnetic flux ψ, velocity parallel to

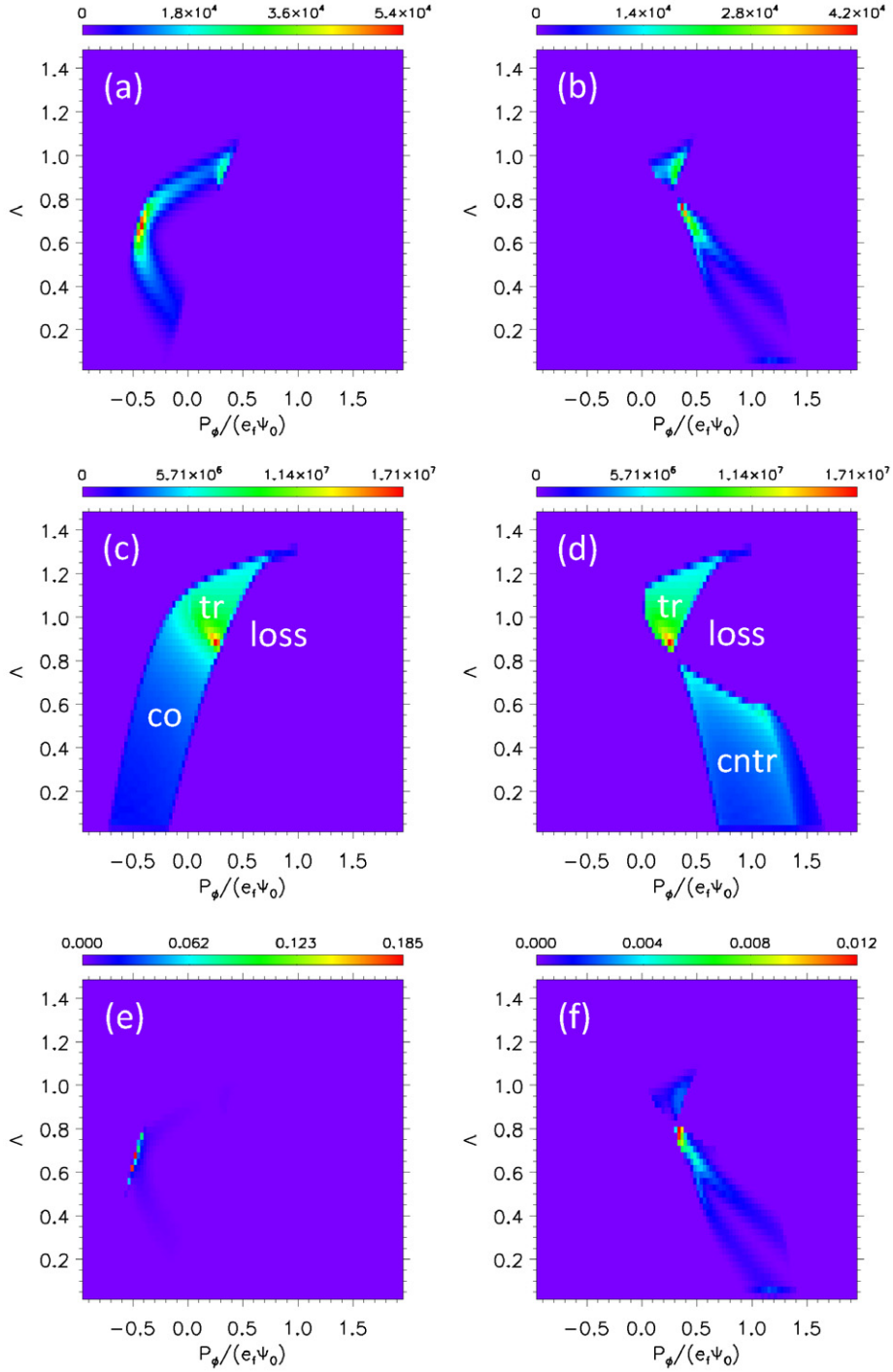

Figure 2. Beam deposition profile in (P_φ, Λ) space for the full-energy component, (a) number of particles (N), (c) phase space volume (V) and (e) distribution function (N/V) for particles co-going to the plasma current, and (b), (d), (f) are the same for the counter-going particles. Phase space regions of co-passing particles (co), counter-passing particles (cntr), trapped particles (tr) and lost trapped particles (loss) are labelled in (c) and (d).

the magnetic field $v_\parallel$, toroidal component of the unit vector of magnetic field b_φ, and $\Lambda \equiv \mu B_0/E$ is pitch-angle variable defined with magnetic moment μ, magnetic field strength at the plasma centre B_0, and particle kinetic energy E. The poloidal flux is taken to be $\psi = 0$ at the plasma centre and $\psi = \psi_0 > 0$ at the plasma edge. We have chosen the sign of poloidal flux opposite to that in the DIII-D experiment. This choice does not affect the physics. We should distinguish the direction of particle motion with respect to the plasma current. The number of deposited beam particles $(= N)$ is shown in figures 2(a) and (b), the Jacobian of the (P_φ, Λ) space $(= V)$ in figures 2(c) and (d), and the beam deposition profile in phase space $(= N/V)$ in figures 2(e) and (f) for particles co- and counter-going to the plasma current, respectively. Particle losses are assumed to take place at the plasma boundary $(r/a = 1)$. The values in the figure are set to be 0 for the particle

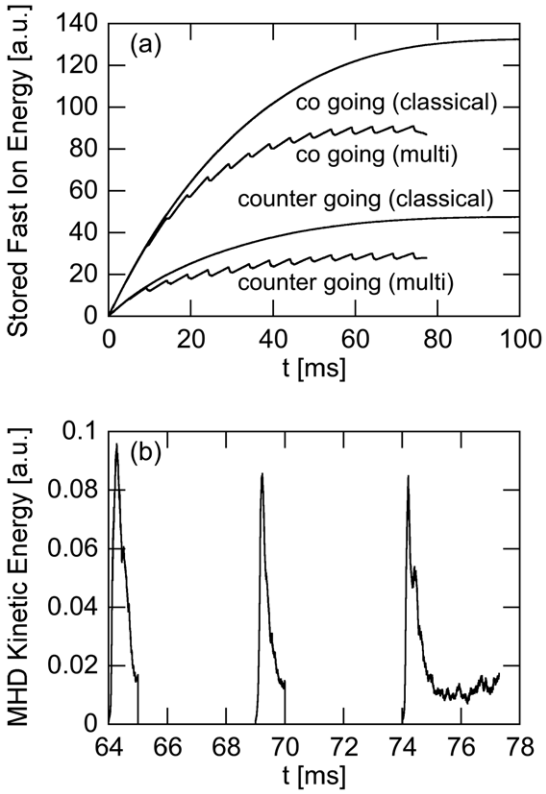

Figure 3. Time evolutions of (*a*) stored fast ion energy in multi-phase and classical simulations and (*b*) MHD kinetic energy in the multi-phase simulation.

loss regions. We see in figures 2(*c*) and (*d*) the confinement regions of co-passing particles, counter-passing particles, and trapped particles labelled 'co', 'cntr', and 'tr', respectively. The trapped region is shown for both the co- and counter-going particles. The horizontal axis in figure 2 is normalized by $e_f\psi_0$. If the particle velocity is negligibly small, the confined regions of co- and counter-going particles overlap each other with $P_\varphi = 0$ at the plasma centre and $P_\varphi = 1$ at the edge. The beam injection energy of ~80 keV, however, separates the phase space regions of co- and counter-going particles.

We see in figures 2(*e*) and (*f*), the distribution function of the beam deposition is highly localized in phase space. The classical distribution function of fast ions is formed from the beam deposition profile after collisions with the bulk plasma particles. The beam deposition profile localized in Λ direction indicates that pitch-angle scattering should be taken into account in addition to slowing down. For the slowing down process of energetic particles, a delta-f simulation model was developed using an analytical time-dependent classical distribution function [13]. However, it is not feasible to construct an analytical distribution function that is consistent with pitch-angle scattering, and pitch-angle scattering is not taken into account in [13]. On the other hand, the full-f method is straightforward for realistic simulations with collisions and has been previously implemented in the MEGA code [24]. In this work, we introduce slowing down, pitch-angle scattering, and energy diffusion with realistic physics parameters for the DIII-D experiment using the full-f method.

Collisions of fast ions with thermal electrons and ions [25] are implemented in the MEGA code. The slowing down is

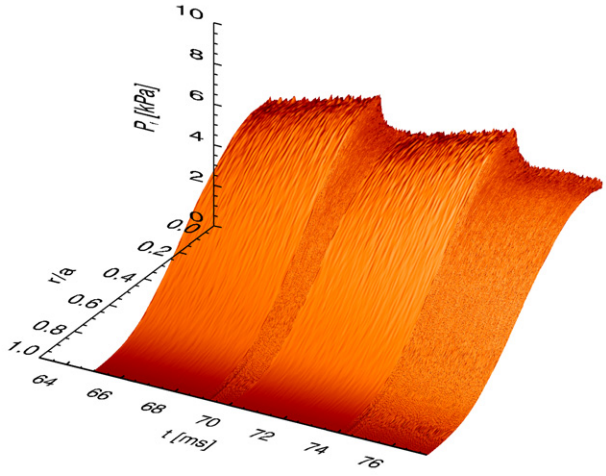

Figure 4. Time evolution of fast ion pressure profile in multi-phase simulation.

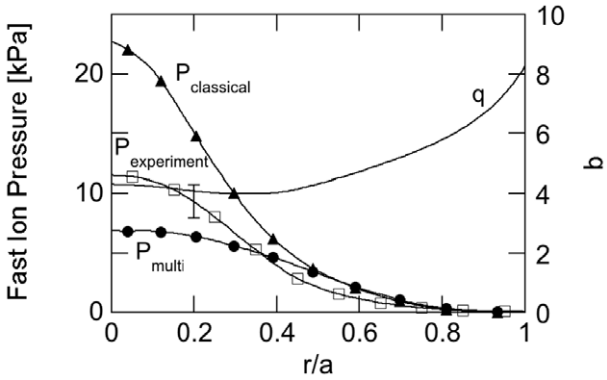

Figure 5. Comparison of fast ion pressure profile among multi-phase simulation (circle), classical (triangle) simulation and experiment (square) with an error bar shown in the figure. The random error in the experimental fast-ion pressure associated with subtraction of the thermal pressure is represented by the error bar; the uncertainty in determination of the total pressure from equilibrium reconstructions contributes a comparable systematic error.

included in the time integration of total particle velocity v by

$$\left(\frac{\mathrm{d}v}{\mathrm{d}t}\right)_{\text{slowing down}} = -\nu\left(v + \frac{v_c^3}{v^2}\right), \tag{8}$$

where ν is drag rate (inverse of the slowing down time) and v_c is the critical velocity above which the fast ion collisions with electrons dominate the slowing down process. Pitch-angle scattering and energy diffusion are taken into account at the end of each time step using a Monte Carlo procedure [26], where a particles' pitch $\lambda = v_\parallel/v$ and total velocity v is altered according to the relations

$$\lambda_{\text{new}} = \lambda_{\text{old}}(1 - 2\nu_d\Delta t) \pm \left[(1-\lambda_{\text{old}}^2)2\nu_d\Delta t\right]^{1/2}, \tag{9}$$

$$v_{\text{new}} = v_{\text{old}} + \frac{\nu\Delta t}{m_f v_{\text{old}}}\left[T_e - \frac{1}{2}T_i\left(\frac{v_c}{v_{\text{old}}}\right)^3\right] \pm \left\{\frac{\nu\Delta t}{m_f}\left[T_e + T_i\left(\frac{v_c}{v_{\text{old}}}\right)^3\right]\right\}^{1/2}, \tag{10}$$

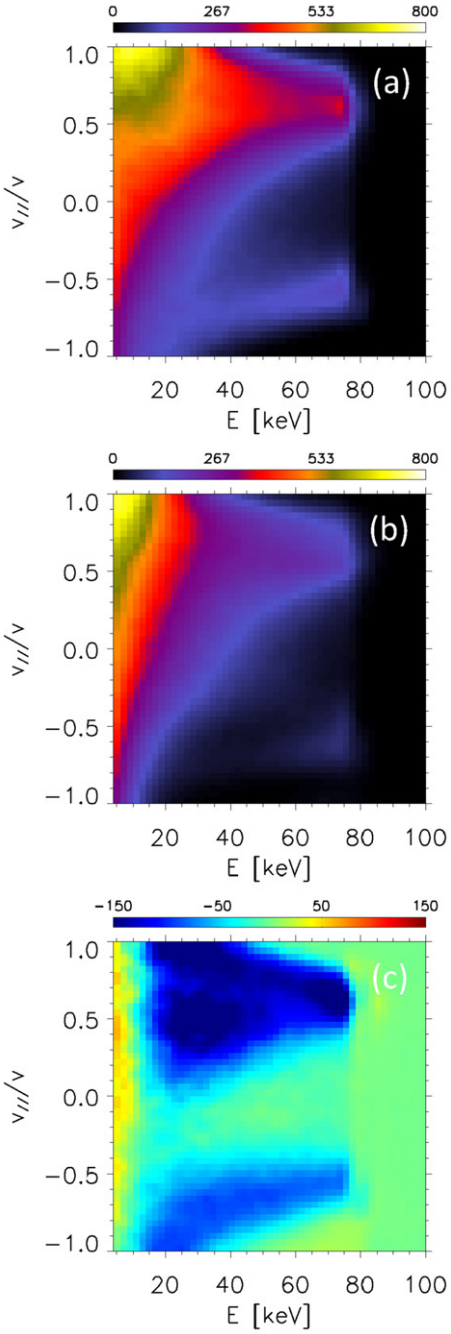

Figure 6. Fast ion distributions in $(E, v_\parallel/v)$ space at $t = 77$ ms in (a) classical simulation, (b) multi-phase simulation. The difference between the two simulations is shown in (c).

where ν_d is the pitch-angle scattering rate, Δt is the time step width, T_e, T_i are respectively electron and ion temperature, and $\pm$ denotes a randomly chosen sign with equal probability for plus and minus.

2.3. Multi-phase simulation

We would like to investigate a fast ion distribution formation process with beam injection, collisions, losses and transport due to the AE modes. A complicating factor is that the time scale of the classical processes without MHD perturbations is

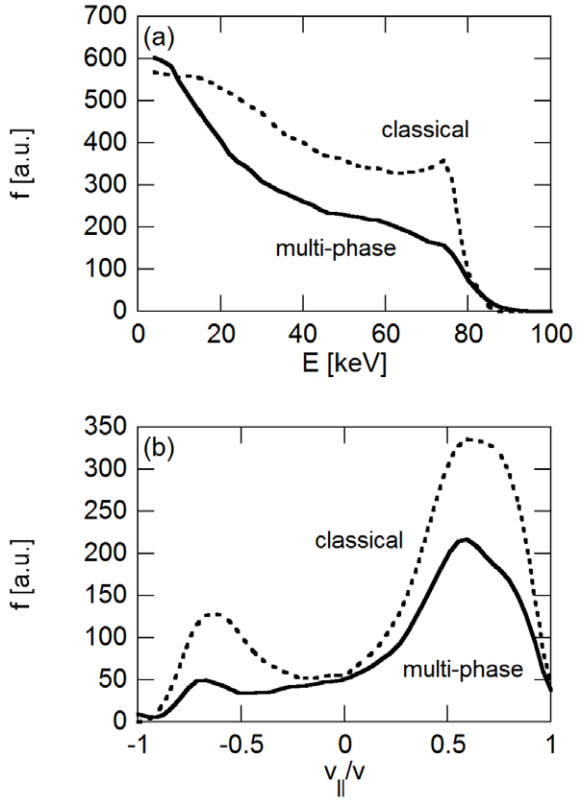

Figure 7. Comparison of fast ion distribution at $t = 77$ ms between multi-phase and classical simulations as functions of (a) energy with $v_\parallel/v = 0.63$ and (b) pitch with $E = 60$ keV.

the slowing down time, which is roughly 200 ms, and longer by four orders of magnitude than the typical oscillation period of AE mode ∼0.02 ms. The time step width is limited by the Courant condition for fast magnetosonic waves in the hybrid simulation. On the other hand, in the classical simulation, the time step width can be taken to be 30 times greater than that in the hybrid simulation. To deal with this efficiently, we construct a multi-phase simulation where we run alternately the classical simulation and the hybrid simulation. In the classical phase of the simulation, the fast ion distribution is built up with the beam injection and collisions. In the subsequent hybrid phase, the built-up fast ion distribution destabilizes AE modes leading to the relaxation of the distribution. We should note that the classical processes, beam injection and collisions, take place also in the hybrid phase. We repeat this combination of the classical and hybrid simulations until the stored fast ion energy is saturated. After which, we continuously run the hybrid simulation to investigate the fast ion distribution and AE modes, and compare them with those of the experiment.

3. Simulation results

3.1. Multi-phase simulation with realistic parameters

We have run a multi-phase simulation and a classical simulation for the DIII-D discharge #142111 at $t = 525$ ms. We use experimental values for collision frequencies, the beam deposition power 4.95 MW (for the full-energy component), and the beam deposition profile shown in figure 2. Eight

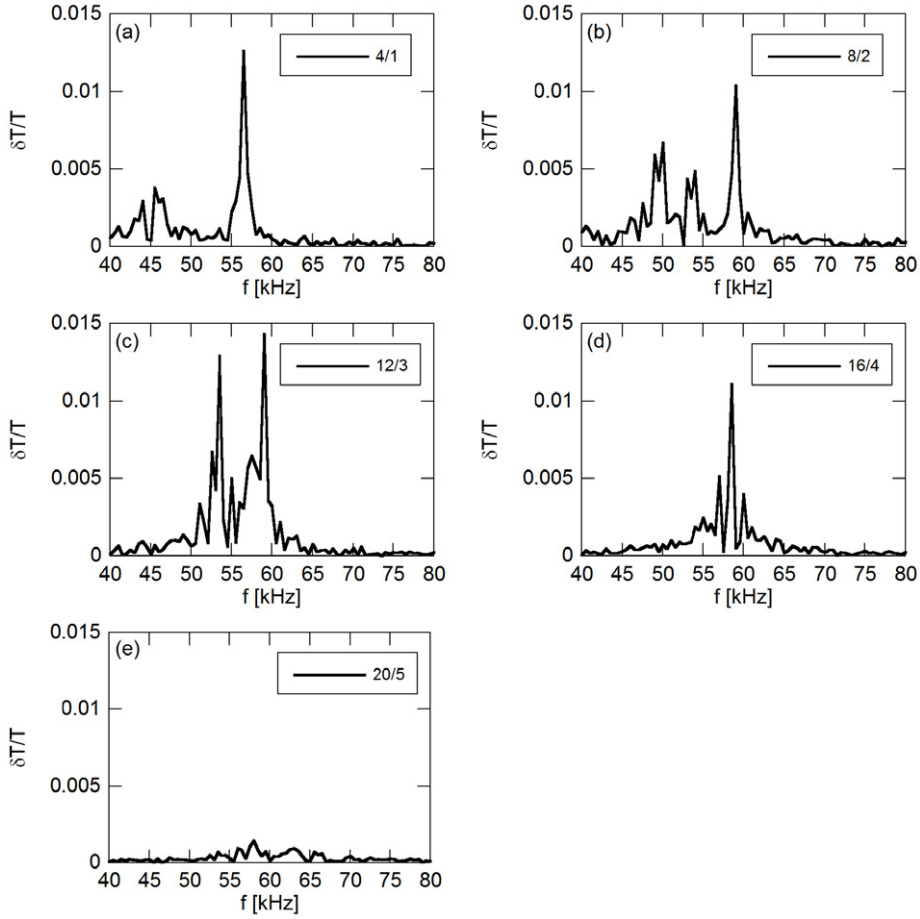

Figure 8. Frequency spectra of temperature fluctuation at $r/a = 0.4$ for 75.0 ms $\leqslant t \leqslant$ 77.3 ms for (*a*) $m/n = 4/1$, (*b*) $m/n = 8/2$, (*c*) $m/n = 12/3$, (*d*) $m/n = 16/4$ and (*e*) $m/n = 20/5$.

million computational particles are injected at a constant rate over a 150 ms time interval, although both the multi-phase and classical simulations are terminated before $t = 150$ ms. The numbers of grid points are (128, 128, 256) for (R, φ, z) coordinates, respectively. We restrict the toroidal mode number of energetic particle drive in the simulation to $n = 1-5$ in order to reduce the numerical noise. This is supported by the experimental observation that the toroidal mode number of the AE modes is $n = 1-5$ at $t \sim 525$ ms [7]. Here, the dissipation coefficients are set to be $5 \times 10^{-7} v_A R_0$. The dependence on the dissipation coefficients is discussed in section 3.3. Figure 3 shows the time evolution of stored fast ion energy and MHD kinetic energy. The multi-phase simulation in figure 3 was run with alternating classical phase for 4 ms and hybrid phase for 1 ms. This combination was repeated until stored fast ion energy is saturated at $t = 75$ ms, after which, the hybrid simulation is run continuously. We see the MHD kinetic energy reaches a steady level in figure 3(*b*). The time evolution of the fast ion pressure profile is shown in figure 4. The fast ion pressure reaches a steady-state profile after $t = 75$ ms. Figure 5 compares the fast ion pressure profiles among the multi-phase and classical simulations, and the experiment. The fast ion pressure profile in the experiment is inferred from the equilibrium reconstruction and the subtraction of the thermal pressure. We see in figure 5 that significant flattening of fast ion pressure profile takes place in the multi-phase simulation. The fast ion profile in the multi-phase simulation is more flattened than that in the experiment. We should note that the half and third energy components, which would increase the fast ion pressure to a level closer to the experiment, are not included in the present simulations, and the total beam deposition power is lower than in the experiment. Figure 6 compares beam distributions in velocity space $(E, v_\parallel/v)$ at $t = 77$ ms between the classical and multi-phase simulations. The positive pitch $v_\parallel/v > 0$ is co-going to both the magnetic field and the plasma current in the equilibrium used in this simulation. What is important is the positive pitch is co-going to the plasma current. We see the distribution function is reduced in the multi-phase simulation. Figure 7 shows the distribution functions versus energy and pitch. We see in figure 7(*a*) the classical distribution has positive gradient for energy just below the injection energy 80 keV. In the multi-phase simulation, the distribution is monotonically decreasing in energy. In figure 7(*b*) the distribution gradient is reduced in pitch in the multi-phase simulation. The modification of the fast ion distribution in the multi-phase simulation is brought about by the interaction with the AE modes, which are discussed in the next subsection.

The collisional heating power of fast ions at $t = 128$ ms in the classical simulation is 3.43 MW, which is lower than the beam deposition power 4.95 MW. Both the prompt losses and the collisional losses at $r/a = 1$ results in the power loss of

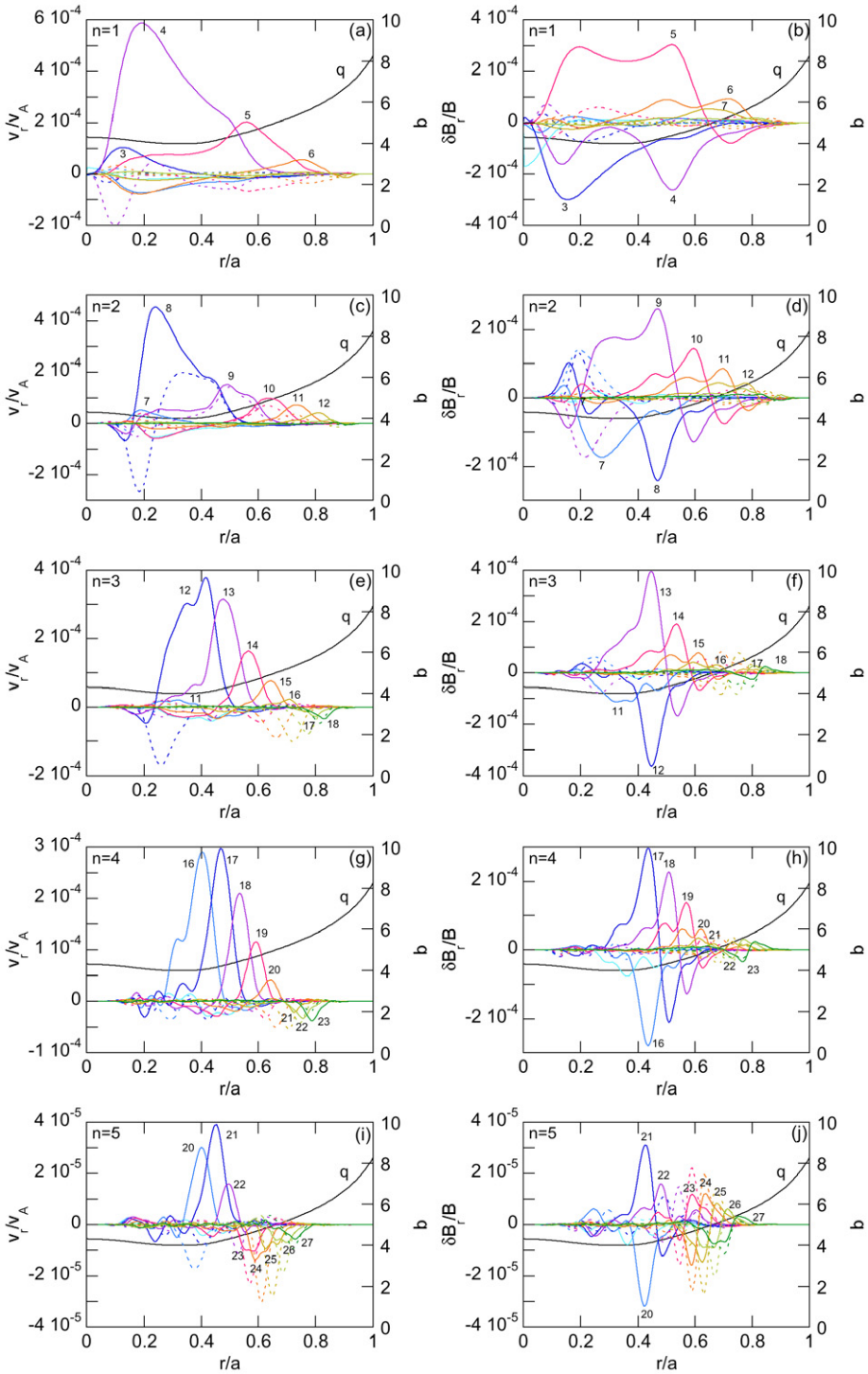

Figure 9. Radial velocity and magnetic fluctuation profiles of TAE modes with toroidal mode number and frequency (*a*), (*b*) $n = 1$, $f = 56.5$ kHz, (*c*), (*d*) $n = 2$, $f = 59.0$ kHz, (*e*), (*f*) $n = 3$, $f = 59.0$ kHz, (*g*), (*h*) $n = 4$, $f = 58.5$ kHz, (*i*), (*j*) $n = 5$, $f = 58.0$ kHz. Solid (dotted) lines represent cosine (sine) components with poloidal mode number labelled in the figure.

1.52 MW. In the multi-phase simulation, the collisional heating power and the power transfer to the AE modes are respectively 2.67 MW and 0.56 MW at $t = 77$ ms. The collisional heating power is reduced by 0.76 MW from the classical heating power due to the interaction with the AE modes. As the energy transferred to the AE modes is further transferred to the bulk plasma through the mode damping, the reduction in the total heating power due to the AE modes is 0.20 MW.

3.2. AE modes and fast ion transport in steady state

Bulk temperature fluctuation spectra with toroidal mode number $n = 1 - 5$ at $r/a = 0.4$ are shown for 75 ms $\leqslant t \leqslant$ 77.3 ms in figure 8. The temperature fluctuation is normalized by the equilibrium temperature. At $t = 525$ ms in the experiment, the TAE modes with $n = 1$ and 3–5 are observed, whereas the $n = 2$ TAE mode is not. We should

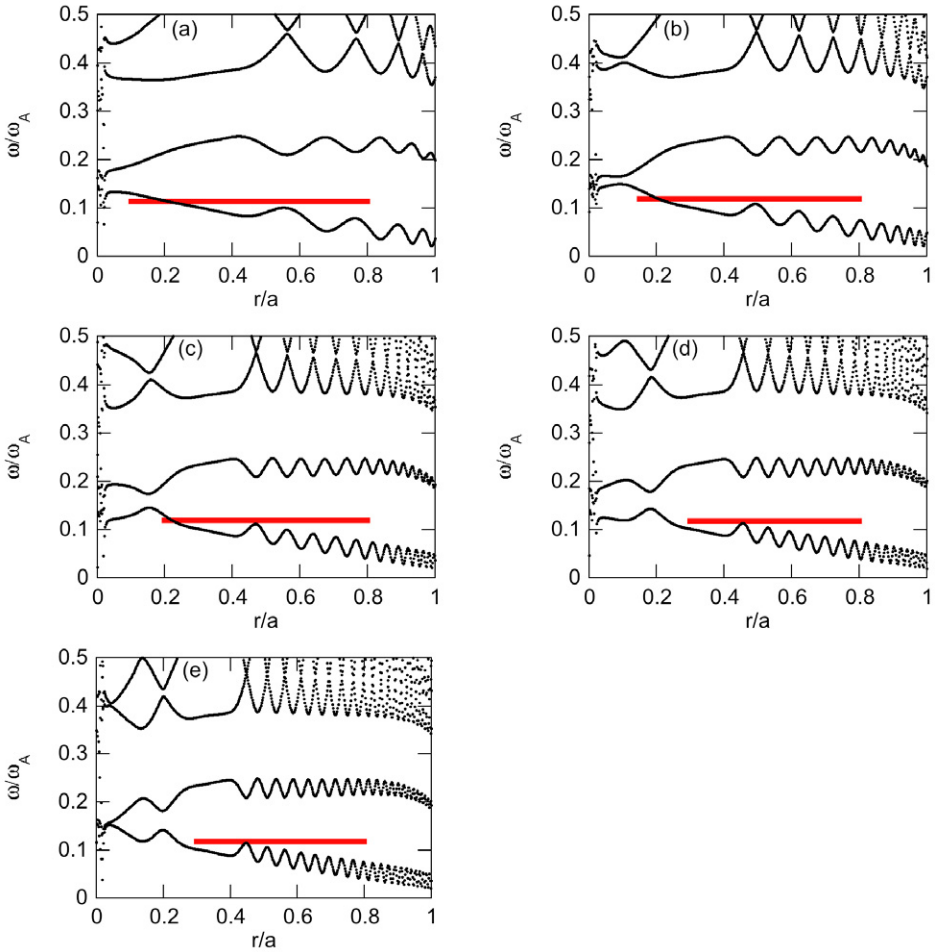

Figure 10. Alfvén continuous spectra for toroidal mode number (*a*) $n = 1$, (*b*) $n = 2$, (*c*) $n = 3$, (*d*) $n = 4$ and (*e*) $n = 5$. Frequency and spatial location of the TAE modes are shown with horizontal line.

note that $n = 2$ modes are observed at other times in this discharge. We see $\delta T/T \sim O(10^{-2})$ for $n = 1$, 3 and 4 that is comparable to the experiment. For $n = 5$, the temperature fluctuation $\delta T/T \sim O(10^{-3})$ is lower than that of the experiment. The frequency of the dominant fluctuations is ∼60 kHz that corresponds to the TAE gap. The spatial profiles of the radial velocity and magnetic fluctuations are analysed for the dominant frequency of each toroidal mode number, and are shown in figure 9. The Fourier decomposition is executed in time for 75 ms $\leqslant t \leqslant$ 77.3 ms. Figure 10 shows the Alfvén continua and the frequency and spatial location of the dominant fluctuations. The Alfvén continua were analysed based on the ideal MHD model with plasma compressibility. The MHD pressure used in the analysis is the sum of thermal pressure and fast ion pressure. The spatial profiles shown in figure 9 consist of many poloidal harmonics, and the frequency is just above the accumulation point of the lower frequency continuum of the TAE gap. These indicate that the dominant fluctuations are TAE modes. The $n = 1$ and 2 modes have also a property like energetic particle mode such that their peak is located on the continuum. The amplitude of the TAE modes is $v_r/v_A \sim \delta B_r/B \sim (3-6) \times 10^{-4}$ for $n = 1-4$ and $v_r/v_A \sim \delta B_r/B \sim 4 \times 10^{-5}$ for $n = 5$. From this, we can conclude that the fast ion profile is flattened by the multiple AE modes with amplitude $v_r/v_A \sim \delta B_r B \sim O(10^{-4})$.

We analyse the fast ion particle flux brought about by the AE modes. Figure 11 shows the radial particle flux at $t = 75$, 76 and 77 ms for each toroidal mode number n

$$F_n(r) = \int_0^{2\pi} \left[n_{f_n} v_{Ern} + (n_f v_\parallel)_n \delta b_{rn} \right] \sigma_n r \, \mathrm{d}\theta \quad (\sigma_{n=0} = 1, \sigma_{n\neq 0} = \tfrac{1}{2}), \tag{11}$$

where n_f, $\delta(n_f v_\parallel)$, v_{Er}, and δb_r are fast ion density, fast ion parallel flow, radial $E \times B$ drift velocity, radial fluctuation of magnetic field unit vector, and the subscript n is toroidal mode number. We found the toroidal mode numbers $n = 1-4$ contribute substantially to the fast ion transport for $0.2 \leqslant r/a \leqslant 0.8$. The level of the total particle flux is about 10^{-8} in the unit of the figure and kept roughly constant over the two intervals. The profile of the total flux, however, varies in time. The magnitude and profile of each flux component show a greater variation than the total flux. The time variation of the particle flux is in contrast to the steady fast ion pressure profile in 75 ms $\leqslant t \leqslant$ 77.3 ms shown in figure 4.

3.3. Dependence on dissipation coefficients and duration of classical phase

Since the employed MHD model lacks a complete physical description that includes kinetic damping of AEs, we employ artificial dissipation coefficients to control the damping. In

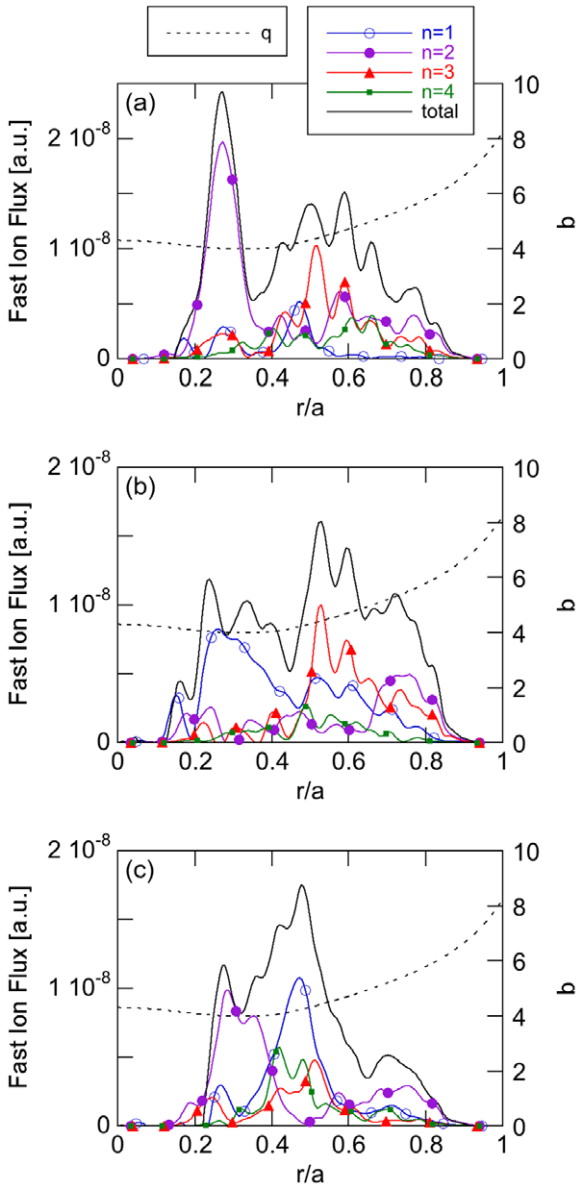

Figure 11. Total fast ion flux brought about by AE modes summed over $n = 0$–5 (solid line) and q-profile (dashed line) for (*a*) $t = 75$ ms, (*b*) $t = 76$ ms and (*c*) $t = 77$ ms. Flux for each toroidal mode number is shown for $n = 1$ (open circle), $n = 2$ (solid circle), $n = 3$ (triangle) and $n = 4$ (square).

addition to the multi-phase simulation described in the previous subsections, we have run two multi-phase simulations with dissipation coefficients $2 \times 10^{-6} v_A R_0$ and $5 \times 10^{-6} v_A R_0$. The stored fast ion energy reaches to steady levels in both the runs at $t = 75$ ms and 80 ms, respectively. The hybrid simulation follows each multi-phase simulation. Figure 12 compares fast ion pressure profiles and MHD kinetic energy evolution in the hybrid simulation for the different dissipation coefficients. We see in figure 12(*a*) that significant flattening of the fast ion profile takes place for all the dissipation coefficients over a range of one order of magnitude. The stored fast ion energy is higher for the larger diffusion coefficients which lead to higher damping rate of the AE modes. The horizontal axis of figure 12(*b*) is the time with offset at the start of the

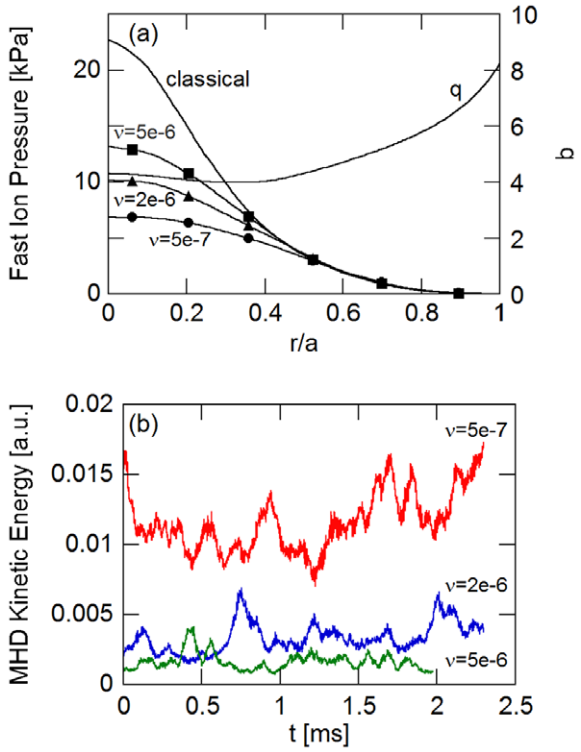

Figure 12. Comparison among different dissipation coefficients for (*a*) fast ion pressure profile and (*b*) time evolution of MHD kinetic energy in the connecting hybrid simulation. Fast ion pressure profile in classical simulation and q-profile are also shown in (*a*). Dissipation coefficients are labelled in the figure.

connecting hybrid simulation. The MHD kinetic energy is lower for the higher dissipation coefficients. MHD kinetic energy for dissipation coefficients $5 \times 10^{-6} v_A R_0$ is lower than that for $5 \times 10^{-7} v_A R_0$ by one order of magnitude. The MHD energy dissipation rate is comparable among the three cases because energy dissipation rate is roughly in proportion to the product of dissipation coefficients and MHD fluctuation energy. For the steady states where AE amplitudes are kept at constant levels, this indicates the energy transfer rate from fast ions to AEs is also comparable among the three cases. Since the temporal variations of particle energy and toroidal canonical momentum are in proportion to each other for the interaction with a wave of constant amplitude, frequency, and toroidal mode number, this indicates the fast ion transport due to the AEs is comparable among the three cases. Our observation that the energy dissipation rate is comparable among the different dissipation coefficients is consistent with figure 12(*a*) that shows the significant flattening of fast ion profile takes place for all the three cases.

Another interesting question is to what extent the multi-phase simulation results depend on the choice of duration for the classical and hybrid phases. Since a full hybrid simulation is too computationally demanding for realistic collision frequencies, we compare our 4 ms classical phase runs with 9 ms for classical phase and 1 ms for hybrid phase. Again, the hybrid simulation is connected to the multi-phase simulation at $t = 75$ ms. This run is the same as the standard run presented in the previous subsections except for the classical phase duration. Figure 13(*a*) compares time

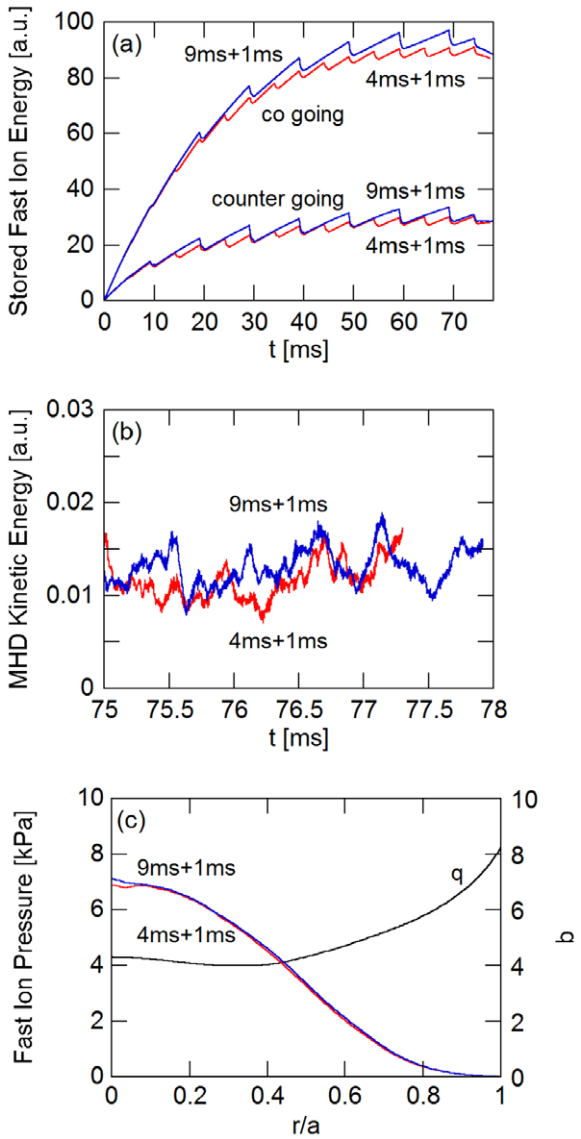

Figure 13. Comparison between multi-phase simulation results with different durations of classical phase 4 and 9 ms for (*a*) stored fast ion energy evolution, (*b*) MHD kinetic energy evolution in the connecting hybrid simulation and (*c*) fast ion pressure profile at $t = 77.3$ ms. The duration of hybrid phase is 1 ms in both simulations.

evolution of stored fast ion energy between the two multi-phase simulations with classical phase for 4 ms and for 9 ms. For co-going particles, the stored fast ion energy is slightly higher in the run with 9 ms classical phase. This suggests a longer duration of the hybrid phase is needed to relax the fast ion distribution built-up during the classical phase. However, for counter-going particles, we see good agreement between the two runs at the end of each hybrid phase. This indicates the duration of hybrid phase 1 ms is enough for the relaxation of the counter-going particle distribution. We would like to point out the stored energy of co-going particles is very close to each other at the end of the simulations. Figures 13(*b*) and (*c*) compare the time evolution of MHD kinetic energy and the fast ion pressure profiles. We see very good agreement between the two runs.

The comparison between the two runs with classical phase duration 4 and 9 ms suggest the following for an entirely hybrid simulation that is equivalent to a multi-phase simulation with classical phase duration 0 ms. In the entirely hybrid simulation, the stored fast ion energy and the fast ion pressure would be lower than those of the multi-phase simulations presented in this paper, because the stored fast ion energy is lower with the classical phase duration 4 ms than with the duration 9 ms. This can be also inferred from the fact that the stored fast ion energy is slowly decreasing at the end of the simulations as shown in figure 13(*a*). However, as already mentioned, we only found a slight difference between the classical phase durations 4 and 9 ms. We do not expect any significant difference in the entirely hybrid simulation. Our conclusion that the fast ion profile is flattened by the multiple AE modes with amplitude $v_r/v_A \sim \delta B_r B \sim O(10^{-4})$ would not change in the entirely hybrid simulation.

3.4. Effects of history and multiple modes

The temperature fluctuation spectrum of $n = 3$ mode shown in figure 8(*c*) has another peak at frequency around 54 kHz lower than that of the primary TAE mode. To understand the lower frequency peak, we have continued the standard run reported in sections 3.1 and 3.2 with all the MHD fluctuations transiently set to be zero at $t = 77.3$ ms. Figure 14 shows the temperature fluctuation spectra at 77.3 ms $\leqslant t \leqslant$ 81.1 ms. The spectra shown in figure 14 are similar to figure 8, but we notice a few differences. The primary peak of $n = 3$ fluctuation at frequency 59 kHz shown in figure 14(*c*) is stronger than in figure 8(*c*), while the secondary peak at frequency 54 kHz is weaker. The time evolution of radial MHD velocity with $m/n = 12/3$ is shown in figure 15(*a*). We see an amplitude oscillation with frequency ~5 kHz. The peak at lower frequency 54 kHz shown in figure 14(*c*) can be attributed to this amplitude oscillation. Figure 15(*b*) displays the time evolution of poloidal flow with $m/n = 0/0$ (zonal flow), of which spatial profile is shown in figure 16 along with that of the poloidal magnetic fluctuation with toroidal mode number $n = 0$. We do not see any clear temporal correlation between the radial MHD velocity and zonal flow in figure 15. The amplitude oscillation of the radial MHD velocity shown in figure 15(*a*) may be caused by the nonlinear wave–particle interaction. In the standard run, the hybrid simulation started at $t = 74$ ms after the classical simulation was run for 4 ms. This makes the MHD fluctuation transiently reach a level substantially higher than the steady level as shown in figure 3(*b*). The interaction with large-amplitude TAE modes generates a large fluctuation in the fast ion distribution function. This may lead to the amplitude oscillation of TAE modes and affect the frequency spectra of MHD fluctuations. In figure 14, the amplitude of $n = 1$ and 2 are reduced from those shown in figure 8. We should be careful of the effect of history when we discuss the details of the frequency spectrum. The stored fast ion energy decreases by 2% from $t = 77.3$ to 81.1 ms. The MHD fluctuations with the spectrum shown in figure 14 are strong enough for transport to keep the fast ion distribution flattened.

We show in figure 16 the spatial profiles of poloidal velocity and poloidal magnetic fluctuation with toroidal mode

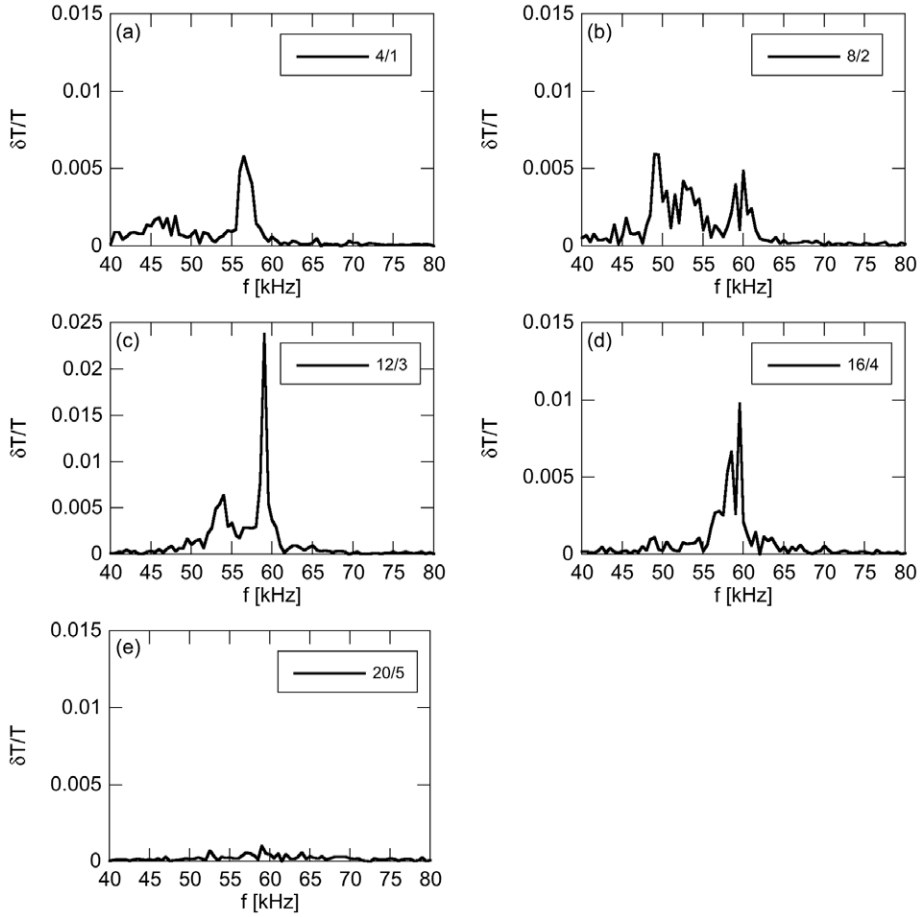

Figure 14. Frequency spectra of temperature fluctuation at $r/a = 0.4$ for 77.3 ms $\leqslant t \leqslant$ 81.1 ms for (*a*) $m/n = 4/1$, (*b*) $m/n = 8/2$, (*c*) $m/n = 12/3$, (*d*) $m/n = 16/4$ and (*e*) $m/n = 20/5$.

number $n = 0$ at $t = 81.1$ ms. The amplitude of zonal flow and field with $m/n = 0/0$ are $\sim 10^{-4}$ normalized by the Alfvén velocity and the toroidal magnetic field, respectively. The comparable amplitude of zonal flow and field is consistent with the result of the hybrid simulation using MEGA [27]. The large amplitude of $m/n = 1/0$ magnetic fluctuation can be attributed to the change of equilibrium due to the dissipation of MHD fluctuations that enhances the MHD pressure. We have carried out another run succeeding the standard run at $t = 77.3$ ms with a numerical filter applied to remove the MHD fluctuations other than $n = 3$. All the MHD fluctuation amplitude including $n = 3$ mode are instantaneously set to be zero at $t = 77.3$ ms. The time evolution of radial velocity fluctuation with $m/n = 12/3$ is shown in figure 17(*a*). We see the amplitude of radial velocity shown in figure 17(*a*) is lower than that in figure 15(*a*). This indicates the multiple modes included in the run shown in figure 15(*a*) enhance the TAE mode amplitude. This enhancement can be attributed to the resonance overlap. The temperature fluctuation spectrum is shown in figure 17(*b*). Comparing with figure 14(*c*) where all the toroidal mode numbers are included for the MHD fluctuations, we see in figure 17(*b*) the $n = 3$ mode amplitude is reduced and there the sharp peak in the frequency spectrum is absent. The reason for the absence of the sharp peak in the frequency spectrum of the single-*n* run remains to be identified. The stored fast ion energy increases by 3% from $t = 77.3$ to 80.2 ms. This indicates that the fast ion transport due to only $n = 3$ fluctuations is not strong enough to maintain the fast ion distribution flattened by the multiple-*n* modes.

4. Discussion and summary

We have developed a multi-phase simulation that is a combination of classical and hybrid simulations for energetic particles interacting with an MHD fluid to simulate the nonlinear dynamics on slowing down time scales of the energetic particles. The hybrid simulation code MEGA is extended with realistic beam deposition profiles, collisions and losses, and is used for both the classical and hybrid phases. The code is run without MHD perturbations in the classical phase, while the interaction between the energetic particles and the MHD fluid is simulated in the hybrid phase. In a multi-phase simulation of DIII-D discharge #142111, the stored fast ion energy is saturated due to Alfvén eigenmodes at a level lower than in the classical simulation. After the stored fast ion energy is saturated, the hybrid simulation is run continuously. It is demonstrated that the fast ion spatial profile is significantly flattened due to the interaction with the multiple AEs with amplitude $v/v_{\mathrm{A}} \sim \delta B/B \sim O(10^{-4})$. The dominant modes found are TAEs, which is consistent with the experimental observation at the simulated time. The $n = 1$ and 2 modes have also a property like energetic particle mode such that

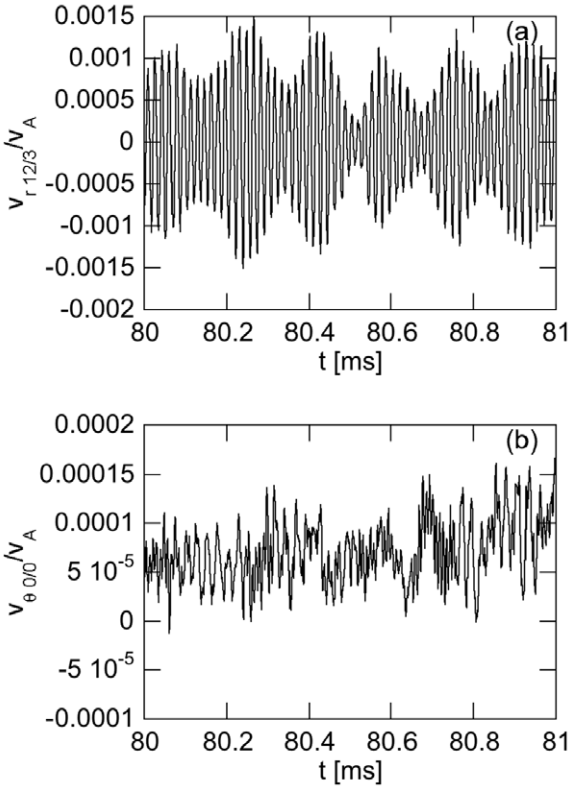

Figure 15. Time evolution of (*a*) radial velocity with $m/n = 12/3$ and (*b*) poloidal velocity with $m/n = 0/0$ at each peak location.

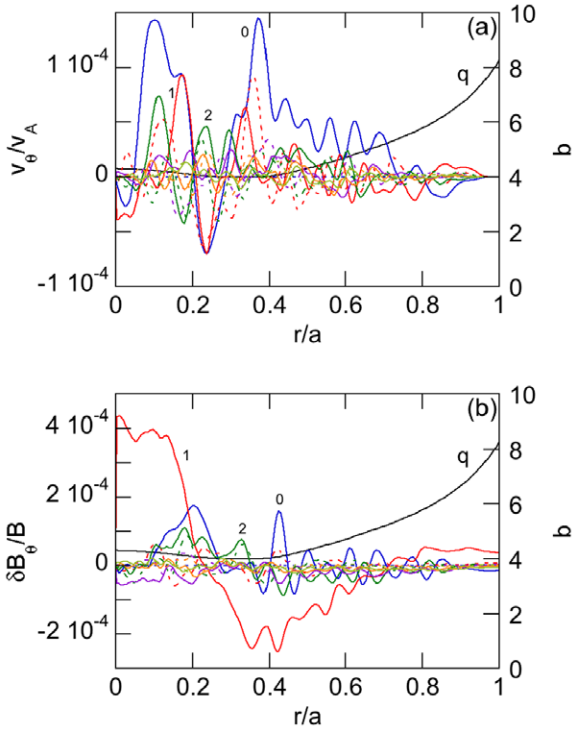

Figure 16. Spatial profiles of (*a*) poloidal velocity and (*b*) poloidal magnetic fluctuation with toroidal mode number $n = 0$ at $t = 81.1$ ms. Solid (dotted) lines represent cosine (sine) components with poloidal mode number labelled in the figure.

their peak is located on the continuum. The amplitude of the temperature fluctuations brought about by the TAEs is of the order of 1% of the equilibrium temperature which is comparable to electron cyclotron emission measurements in the experiment. In the standard run, the amplitude of the TAE modes is $v_r/v_A \sim \delta B_r/B \sim (3-6) \times 10^{-4}$ for $n = 1-4$, and the fast ion pressure profile is more flattened than that in the experiment. We expect that the half and third energy beam components, which are not included in the present simulations with the beam deposition power 4.95 MW, would increase the beam deposition power to 6.25 MW and make the fast ion pressure closer to the experiment.

We carried out two more multi-phase simulations with different dissipation coefficients. Significant flattening of fast ion spatial profile takes place over a range of one order of magnitude for the dissipation coefficients. The kinetic energy of the MHD fluctuations is roughly in proportion to the inverse of the dissipation coefficients. This is consistent with the result that the significant flattening of fast ion spatial profile takes place for all the dissipation coefficients. The physics model in this study does not include kinetic damping of AE modes such as radiative damping [19] and thermal ion Landau damping. The dissipation coefficients enable us to control the damping rate, and we can adjust dissipation coefficients to match the experimental fast ion profile. The continuous spectrum shown in figure 10(*b*) indicates that continuum damping takes place for the $n = 2$ mode at $r/a \sim 0.2$. In the radial velocity profile of the $n = 2$ mode shown in figure 9(*c*), the sine part (dashed line) of $m = 8$ harmonic has a sudden variation around $r/a \sim 0.2$, which is consistent with the continuum damping. This indicates that the continuum damping is qualitatively captured in the simulation. However, a quantitative verification of continuum damping has not yet been performed with MEGA code. A perfect reproduction of the AE mode spectrum in the experiment with the absence of the $n = 2$ mode at $t = 525$ ms may need a fully kinetic description of the bulk plasma and also a quantitative verification of continuum damping.

We also performed a second multi-phase simulation with a different classical phase duration (9 ms versus 4 ms) and found good agreement between the two cases. From this, we conclude that if an entirely hybrid simulation was possible on a reasonable timescale, the results would be similar, i.e. a significant flattening of fast ion profile for relatively low AE amplitudes. We investigated the effect of history on the MHD frequency spectra. After all the MHD fluctuation amplitude is transiently set to be zero, the hybrid simulation was continued. We found that the amplitude of the secondary peak at lower frequency is reduced, and the secondary peak is attributed to the amplitude oscillation that is likely to be excited by the nonlinear wave–particle interaction. We should be careful of this effect when we analyse the MHD frequency spectra just after the classical phase, because the AE mode amplitude transiently reaches a high level. In addition, we examined the evolution with only $n = 3$ MHD fluctuations. The amplitude oscillation takes place as well as the standard run where all the MHD fluctuations are included. However, the $n = 3$ mode amplitude is reduced and there the sharp peak in the frequency spectrum is absent. In the multiple-n run, the resonance overlap may enhance the amplitude of TAE modes. The reason for the absence of the sharp peak in the frequency spectrum of the single-n run remains to be identified.

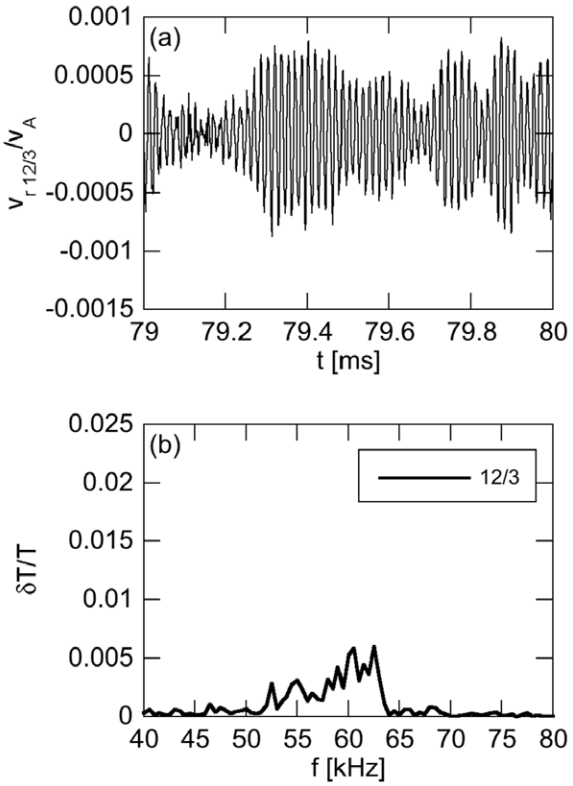

Figure 17. Time evolution of radial velocity with $m/n = 12/3$ (a), and frequency spectra of temperature fluctuation at $r/a = 0.4$ for $77.3\,\text{ms} \leqslant t \leqslant 80.2\,\text{ms}$ for $m/n = 12/3$ (b), in the run where a numerical filter is applied to MHD fluctuations to retain only toroidal mode number $n = 3$.

Two important subjects are under investigation and will be the subject of future publications. The first is a detailed comparison of temperature fluctuations between simulation and experiment. In the DIII-D experiment, ECE measurements revealed the radial profiles of amplitude and phase for the electron temperature fluctuations. We have the bulk plasma temperature fluctuations in the MHD simulations, and a comparison with ECE measurements is straightforward. The half and third energy beam components, which are not included in the present simulations, will be included. Also, the dependence of the electron temperature fluctuation amplitude with the plasma rotation included and/or extended MHD models is also of interest.

The second subject for future work is the fast ion transport due to the multiple AE modes in the steady fast ion distribution. We investigated in this work the fast ion particle flux profile and found it varies in time while the fast ion spatial profile is kept constant. The detailed analysis of the time evolution of fast ion flux profile is needed to understand the fast ion transport due to the multiple AE modes. This issue is closely related to the fast ion losses coherent and incoherent to the AE modes measured by the fast ion loss detectors [6, 28]. With the approach employed here, we can analyse the details of the fast ion transport in both configuration space and velocity space.

Acknowledgments

Numerical computations were performed at the Helios of the International Fusion Energy Center, the Plasma Simulator of National Institute for Fusion Science, and the K Computer of RIKEN Advanced Institute for Computational Science (Project ID: hp120212). This work was supported partly by the JSPS-NRF-NSFC A3 Foresight Program in the field of Plasma Physics (NSFC: No. 11261140328).

References

[1] Heidbrink W.W. *et al* 2007 *Phys. Rev. Lett.* **99** 245002
[2] Van Zeeland M.A. *et al* 2009 *Nucl. Fusion* **49** 065003
[3] White R.B., Gorelenkov N., Heidbrink W.W. and Van Zeeland M.A. 2010 *Plasma Phys. Control. Fusion* **52** 045012
[4] White R.B., Gorelenkov N., Heidbrink W.W. and Van Zeeland M.A. 2010 *Phys. Plasmas* **17** 056107
[5] Tobias B.J. *et al* 2011 *Phys. Rev. Lett.* **106** 075003
[6] Van Zeeland M.A. *et al* 2011 *Phys. Plasmas* **18** 056114
[7] Van Zeeland M.A. *et al* 2012 *Nucl. Fusion* **52** 094023
[8] Spong D.A. *et al* 2012 *Phys. Plasmas* **19** 082511
[9] Vlad G. *et al* 2009 *Nucl. Fusion* **49** 075024
[10] Chen Y. *et al* 2013 *Phys. Plasmas* **20** 012109
[11] Berk H.L., Breizman B.N. and Pekker M.S. 1995 *Nucl. Fusion* **35** 1713
[12] Todo Y., Berk H.L. and Breizman B.N. 2003 *Phys. Plasmas* **10** 2888
[13] Todo Y., Berk H.L. and Breizman B.N. 2012 *Nucl. Fusion* **52** 033003
[14] Park W. *et al* 1992 *Phys. Fluids* B **4** 2033
[15] Spong D.A., Carreras B.A. and Hedrick C.L. 1992 *Phys. Fluids* B **4** 3316
[16] Todo Y., Sato T., Watanabe K., Watanabe T.H. and Horiuchi R. 1995 *Phys. Plasmas* **2** 2711
[17] Briguglio S., Vlad G., Zonca F. and Kar C. 1995 *Phys. Plasmas* **2** 3711
[18] Wang X., Zonca F. and Chen L. 2010 *Plasma Phys. Control. Fusion* **52** 115005
[19] Mett R.R. and Mahajan S.M. 1992 *Phys. Fluids* B **4** 2885
[20] Todo Y. and Sato T. 1998 *Phys. Plasmas* **5** 1321
[21] Littlejohn R.G. 1983 *J. Plasma Phys.* **29** 111
[22] Lao L.L. *et al* 1985 *Nucl. Fusion* **25** 1421
[23] Budny R.V. 1994 *Nucl. Fusion* **34** 1247
[24] Bierwage A., Shinohara K., Aiba N. and Todo Y. 2013 *Nucl. Fusion* **53** 073007
[25] Heidbrink W.W. and Sadler G.J. 1994 *Nucl. Fusion* **34** 535
[26] Boozer A.H. and Kuo-Petravic G. 1981 *Phys. Fluids* **24** 851
[27] Todo Y., Berk H.L. and Breizman B.N. 2012 *Nucl. Fusion* **52** 094018
[28] García-Munoz M. *et al* 2010 *Phys. Rev. Lett.* **104** 185002